Transient Stability Assessment of Multi-Machine Multi-Converter Power Systems

Hugo N. Villegas Pico, *Member, IEEE*, and Brian B. Johnson, *Member, IEEE*

***Abstract*—Transmission faults caused by recent wildfires in California have induced the disconnection of utility-scale converters in photovoltaic (PV) power plants. Postmortem investigations reported that tripping commands were caused by phase-locked loops (PLLs) and dc-side dynamics, which are typically unmodeled in classical transient stability studies. Since existing simulation packages rely on simplified models that neglect these dynamics, they have a limited capability to predict converter behavior during faults. To address this shortcoming, we set forth a positive-sequence model for PV power plants that is derived from physics and controls first principles. As seen on utility-scale three-phase converters, the model includes PLLs, dc-side dynamics, and closed-loop controllers. Instances of the developed model are integrated into illustrative power systems containing conventional generators. Numerical simulations of the obtained multi-machine multi-converter power systems are assessed via a suitable set of stability and performance metrics.**

***Index Terms*—Photovoltaic (PV) systems, power system transients.**

I. Introduction

THE classical transient stability problem pertains to ascertaining whether or not a set of interconnected machines will remain in synchronism after large disturbances [1]–[3]. To address this issue, transient simulation packages were originally conceived to capture a limited range of electromechanical time constants [2], [4], [5]. At the present time, the role of synchronous machines is gradually changing because they are being displaced by converter-based generation [6], [7]. However, experience in integrating significant amounts of converters into modern electric grids is still limited [8, p. vii]. Notably, simulation models may fail to *predict* the actual transient performance of renewable assets which hampers proactive decisions by grid operators [8]–[11].

Manuscript received June 7, 2018; revised October 10, 2018 and January 16, 2019; accepted February 2, 2019. Date of publication March 6, 2019; date of current version August 22, 2019. This work was authored in part by the Alliance for Sustainable Energy, LLC, the Manager and Operator of the National Renewable Energy Laboratory for the U.S. Department of Energy (DOE) under Contract DE-AC36-08GO28308. This work was supported by the DOE's Solar Energy Technologies Office under Contract DE-EE0000-1583. The work of B. B. Johnson was also supported by the Washington Research Foundation. Paper no. TPWRS-00883-2018. *(Corresponding author: Hugo N. Villegas Pico.)*

H. N. Villegas Pico is with the National Renewable Energy Laboratory, Golden, CO 80401 USA (e-mail: HugoNestor.VillegasPico@nrel.gov).

B. B. Johnson is with the Department of Electrical and Computer Engineering, University of Washington, Seattle, WA 98195 USA (e-mail: brianbj@uw.edu).

Color versions of one or more of the figures in this paper are available online at http://ieeexplore.ieee.org.

Digital Object Identifier 10.1109/TPWRS.2019.2898182

Power converters differ in both construction and controls from synchronous machinery, hence they exhibit distinctive dynamics. Converters respond relatively quickly to disturbances because of their power electronic circuitry and absence of moving parts. In general, the closed-loop response of a power converter is dominated by its digital controls. In power electronics applications, closed-loop converter dynamics are often modeled in detail [12]–[15]. Nonetheless, to incorporate converter-based power plants into available transient stability simulations, fast dynamics and internal control loops are commonly simplified [16]. Although this eases model integration into transient stability software, it comes at the expense of simulations that might depart from actual behavior.

A need to satisfactorily simulate the transient performance of converter models is motivated by recent transmission faults that induced the disconnection of renewable assets [8]–[11]. Of particular relevance, the *Blue Cut Fire* in 2016 and the *Canyon Fire 2* in 2017 both had system impacts in the Southern California electric grid: they prompted the disconnection of 1,200 MW [10] and 900 MW [11] of photovoltaic (PV) generation, respectively. Unfortunately, these events were not predicted by available transient simulation tools, suggesting the need for higher fidelity studies [8]. To this end, electromagnetic transient (EMT) analysis can be employed, but their computational complexity is considerably higher compared to positive-sequence methods [17, p. 7]. Publicly available information on these incident reports indicate that some PV plants tripped due of a variety of reasons [8], [10], [11]: (i) off-nominal phase-locked-loop (PLL) frequency, (ii) dc-link overcurrent, or (iii) ac-side converter overvoltage. These findings contrast with converter models in transient stability software where PV plants are modeled using current-controlled sources with electromechanical time constants. See [16, Fig. 4] to note the absence of a PLL and dc-side dynamics.

In wind energy applications, standard representations of wind turbines and controls have been developed for positive-sequence simulations [18]–[21] and are employed to conduct a variety of transient stability studies [21]–[25]. Similar to PV power plants, turbine models disregard dynamics associated with fast-acting subsystems such as the PLL and dc-link [19], [21]. Notably, omission of the PLL in a Type-4 turbine model is known to cause numerical issues [26] which can be avoided by using heuristic PLL models [26]–[28]. In general, model simplifications are considered reasonable when capturing dynamics during the recovery stage only, i.e., *after* a fault has been cleared [18, p. 10]. As revealed in [21], simplified turbine models may be unable to predict actual behavior *during* faults.

To comprehensively predict the transient response of PV power plants while avoiding burdensome computations of EMT studies, we propose the incorporation of higher fidelity models into positive-sequence transient simulations. We focus on the most commonly used three-phase converter structure in industry which is comprised of a single dc-to-ac conversion stage [29]. We also leverage the artifact that synchronous and converter-based generation act as positive-sequence sources [10], [16], [30] and that asymmetric transmission faults can be modeled in the positive-sequence domain [10]. To ascertain transient performance from simulations, we look beyond rotor-angle stability and assess the voltage ride-through (VRT) capability of converter-based generation as mandated by grid codes [31].

This paper specifically provides the following contributions. (i) A voltage-behind-reactance model of a PV power plant that is derived from circuit laws and expressed in a reference frame whose angle and speed is provided by its PLL. This eliminates numerical issues observed in converters that are modeled as ideally-synchronized current sources [26]. In contrast to [26]–[28], the PLL model is incorporated by referring its angle to that of a common synchronous reference frame, and it is consistent with actual PLL implementations [15], [32]. (ii) An iterative scheme with proven convergence guarantees that enables the seamless incorporation of the nonlinear PV array model and dc-link into transient stability studies. The PV array model, which is typically neglected, is necessary to ascertain whether load-generation balance is met after the system recovers from a fault. The dc-link model is also required to capture dc current transients during faults [8], [10], [11]. The proof of convergence assures the analyst that the PV array model will not compromise the numerical simulation. (iii) A set of stability and performance metrics is proposed to ascertain whether conventional and converter-based assets are compromised during faults. In contrast to studies that focus on post-fault recovery [18], [21]–[25], the proposed metrics are useful to assess ac- and dc-side transients both during *and* after network reconfigurations [10], [11]. Overall, this contributions align with state-of-the-art reliability guidelines [8].

The paper is organized as follows. In Section II, preliminaries for dynamic modeling and assessment framework of power systems are outlined. Dynamic models of conventional and PV power plants are derived in Sections III and IV, respectively. In Section V, a multi-machine multi-converter power system for positive-sequence simulation consolidates the models of Sections III and IV. A set of suitable metrics to assess the stability and performance of the power system model of Section V are given in Section VI. In Section VII, two illustrative case studies showcase the contributions of the paper. Concluding statements are provided in Section VIII.

II. Preliminaries

The multi-machine multi-converter dynamics are modeled via a set of coupled ordinary differential equations (ODEs):

$$\frac{d}{dt}x = F_\gamma(x,u) \tag{1}$$

$$y = G_\gamma(x,u) \tag{2}$$

for $t \in [0,T]$, $x(0)=x_0$, $\gamma \in \{1,2,3\}$. The vector $x \in \mathbb{R}^{n_x}$ encapsulates the states of N conventional and K photovoltaic power plants. The input $u \in \mathbb{R}^{n_u}$ represents commands from a grid operator and maximum power point tracking (MPPT) loops of PV power plants. The commands, u, are modeled as constants because they are relatively slow to the transient dynamics of interest. All states and inputs are normalized as per unit variables of appropriate bases, e.g., rated line-to-line voltages, a system volt-ampere base, S_b, and a system speed base, ω_b [3], [33]. A conventional power plant comprises a synchronous generator, excitation system, prime mover, and controls. A PV power plant has an aggregated representation of power converters, PLLs, dc-links, PV arrays, and controls.

Three forms of $F_\gamma : \mathbb{R}^{n_x} \times \mathbb{R}^{n_u} \to \mathbb{R}^{n_x}$, as indexed by γ, represent the positive-sequence transmission topology before ($\gamma=1$), during ($\gamma=2$), and after ($\gamma=3$) a fault. System outputs $y \in \mathbb{R}^{n_y}$ are mapped from states and inputs via the three forms of $G_\gamma : \mathbb{R}^{n_x} \times \mathbb{R}^{n_u} \to \mathbb{R}^{n_y}$. State solution approximations for (1) are obtained via available numerical methods [34], [35]. A numerical solver returns a sequence of vectors $\{x(t_o)\}_{o=0}^{n_o}$, representing states at $t=t_o$ with $t_0=0$ and $t_{n_o}=T$. The simulation horizon, T, can range from 3 s to 15 s [2, p. 15]. To assess stability and performance of the system, a sequence of outputs $\{y(t_o)\}_{o=1}^{n_o}$ are generated from the sequence of states (and inputs) via (2).

Three-phase variables are expressed with *dq*-axis quantities that originate from a reference frame transformation with angular displacement θ_ν and speed $d\theta_\nu/dt = \omega_b\,\omega_\nu$ [13]:

$$\left[\, f_d^\nu,\, f_q^\nu \,\right]^\top = \frac{2}{3} T(\theta_\nu) \left[\, f_a,\, f_b,\, f_c \,\right]^\top. \tag{3}$$

Here, f represents either voltages or currents and:

$$T(\theta_\nu) = \begin{bmatrix} \cos(\theta_\nu) & \cos(\theta_\nu - \frac{2\pi}{3}) & \cos(\theta_\nu + \frac{2\pi}{3}) \\ -\sin(\theta_\nu) & -\sin(\theta_\nu - \frac{2\pi}{3}) & -\sin(\theta_\nu + \frac{2\pi}{3}) \end{bmatrix}. \tag{4}$$

To shorten modeling notation in Section IV, we employ:

$$f_{dq}^\nu := \left[\, f_d^\nu,\, f_q^\nu \,\right]^\top \text{ and } f_{qd}^\nu := \left[\, f_q^\nu,\, -f_d^\nu \,\right]^\top. \tag{5}$$

We consider $1+N+K$ reference frames:

$$\nu \in \{\text{`}e\text{'}, \text{`}r_1\text{'}, \ldots, \text{`}r_n\text{'}, \ldots, \text{`}r_N\text{'}, \text{`}\epsilon_1\text{'}, \ldots, \text{`}\epsilon_k\text{'}, \ldots, \text{`}\epsilon_K\text{'}\}. \tag{6}$$

Index 'e' represents a common synchronous reference frame to model transmission system quantities. Reference frames to represent variables of an n-th conventional or k-th PV power plant are indexed by 'r_n' or 'ϵ_k', respectively.

To couple generation to a transmission network, *dq*-axis variables are transformed to the reference frame 'e' via [13]:

$$f_d^e + \mathsf{j} f_q^e = \mathsf{e}^{\mathsf{j}\delta_\nu} \left(f_d^\nu + \mathsf{j} f_q^\nu \right) \tag{7}$$

where $\delta_\nu = \theta_\nu - \theta_e$, e is the Euler's number, and $\mathsf{j} = \sqrt{-1}$ is the imaginary unit.

III. Conventional Power Plants

A. AC Synchronous Machine

The n-th ($n = 1, \ldots, N$) machine dynamics are [3]:[1]

$$\frac{d}{dt}e_d^{r_n} = -\frac{1}{\tau_{do}^n}(e_d^{r_n} + (X_d^{\prime n} - X_d^n)i_q^{r_n} - e_{fd}^n), \tag{8}$$

$$\frac{d}{dt}e_q^{r_n} = -\frac{1}{\tau_{qo}^n}(e_q^{r_n} - (X_q^{\prime n} - X_q^n)i_d^{r_n}), \tag{9}$$

$$\frac{d}{dt}\omega_{r_n} = \frac{1}{2H^n}\left(T_m^n - e_d^{r_n} i_d^{r_n} - e_q^{r_n} i_q^{r_n}\right), \tag{10}$$

$$\frac{d}{dt}\delta_{r_n} = \omega_b\left(\omega_{r_n} - \omega_e\right). \tag{11}$$

These represent a 1.1-type model with one d-axis field winding, one q-axis damper, and rotor inertia constant H^n. Stator circuit dynamics are neglected. Ac machine reactances are constant because their magnetic saturation is not modeled. We assume $X_d^{\prime n} = X_q^{\prime n}$; however, $X_d^{\prime n}$ and $X_q^{\prime n}$ are not equal even in round-rotor machines. Superscript 'r_n' designates angle displacement of the n-th rotor frame, $d\theta_{r_n}/dt = \omega_b\,\omega_{r_n}$.

The variables $e_{dq}^{r_n}$ represent voltages behind a transient reactance and $i_{dq}^{r_n}$ captures currents injected into the transmission network. The field voltage generated by the exciter is e_{fd}^n. Rotor speed and relative rotor angle states are ω_{r_n} and δ_{r_n}, respectively. The prime mover mechanical torque is T_m^n. The relative dynamics of (11) are obtained by referring the rotor speed, $d\theta_{r_n}/dt$, to the 'e' reference frame speed [3], [33]:

$$\frac{d}{dt}\theta_e = \omega_b\,\omega_e \text{ with } \omega_e = \frac{\sum_{n=1}^N \omega_{r_n} H^n}{\sum_{n=1}^N H^n}. \tag{12}$$

B. DC Excitation System

The n-th exciter, stabilizer, and amplifier dynamics are [3]:

$$\frac{d}{dt}e_{fd}^n = -\frac{1}{\tau_e^n}\left((k_e^n + S_e^n(e_{fd}^n))e_{fd}^n - v_a^n\right), \tag{13}$$

$$\frac{d}{dt}r_f^n = -\frac{1}{\tau_f^n}\left(r_f^n - \frac{k_f^n}{\tau_f^n}e_{fd}^n\right), \tag{14}$$

$$\frac{d}{dt}v_a^n = -\frac{1}{\tau_a^n}\left(v_a^n - k_a^n v_e^n + S_a^n(v_a^n)\right), \tag{15}$$

$$S_e^n(e_{fd}^n) = A^n \mathsf{e}^{B^n\, e_{fd}^n}, \tag{16}$$

$$S_a^n(v_a^n) = \left(k_a^n - v_{a,\mathrm{mx}}^n\right)\left(\frac{v_a^n}{v_{a,\mathrm{mx}}^n}\right)^{\chi}. \tag{17}$$

Here, τ_e^n, τ_f^n, and τ_a^n are exciter, stabilizer, and amplifier time constants, respectively. The parameters $k_e^n = -S_e^n(e_{fd}^n(0))$, k_f^n, and k_a^n correpond to rheostat, stabilizer, and amplifier gains [3, Ch. 4]. Notice the function (16) for given constants, A^n and B^n, models saturation of the exciter iron [3, p. 67].[2] The function (17), with χ an odd integer, models saturation of the voltage amplifier so that $-v_{a,\mathrm{mx}}^n \le v_a^n \le v_{a,\mathrm{mx}}^n$ [36].

The control error:

$$v_e^n = V^{*n} - V^n + r_f^n - \frac{k_f^n}{\tau_f^n}e_{fd}^n \tag{18}$$

is an input to (15), V^{*n} is the reference voltage, and:

$$V^n = \sqrt{(v_q^{r_n})^2 + (v_d^{r_n})^2} \tag{19}$$

is the measured terminal voltage of the n-th machine with [3]:

$$v_d^{r_n} = e_d^{r_n} - r_s^n i_d^{r_n} + X_d^{\prime n} i_q^{r_n} \tag{20}$$

$$v_q^{r_n} = e_q^{r_n} - r_s^n i_q^{r_n} - X_d^{\prime n} i_d^{r_n}. \tag{21}$$

C. Prime Movers

An n-th steam or ideal hydro turbine is modeled with [3]:[3]

$$\frac{d}{dt}T_m^n = \begin{cases} -\frac{1}{\tau_{ch}^n}\left(T_m^n - P_v^n\right) & \text{thermal} \\ -\frac{2}{\tau_w^n}\left(T_m^n - P_v^n + \tau_w^n \frac{d}{dt}P_v^n\right) & \text{hydro}. \end{cases} \tag{22}$$

Their control is accomplished with the speed-droop governor:

$$\frac{d}{dt}P_v^n = -\frac{1}{\tau_v^n}\left(P_v^n - P_v^{*n} + \frac{\omega_{r_n} - 1}{R_d^n}\right). \tag{23}$$

In (22), τ_{ch}^n and τ_w^n are steam chest and water time constants, respectively. In (23), τ_v^n and R_d^n are the valve time constant and speed droop (5% in the unit power base), respectively. The valve position command P_v^{*n} is set by a grid operator. Notice in (22) that the magnitudes of torque T_m^n and valve position P_v^n are similar since they are in per unit. However, they have distinct physical units before per unitization [3, p. 76–82].

IV. Photovoltaic Power Plants

The PV plant model in Fig. 1 is derived from a structure-preserving aggregation of multiple parallel-connected dc-ac converters [29]. Power produced by PV arrays is injected into the grid by a power converter, which regulates ac current delivery into an LCL filter. Active and reactive power, P_R^k and Q_R^k, flow into the grid via a step-up transformer (not shown), with its low-voltage side denoted as a k-th bus. Ac waveforms of the k-th PV power plant are modeled in a 'ϵ_k' reference frame, whose angle, θ_{ϵ_k}, and speed, $d\theta_{\epsilon_k}/dt$, originate from a k-th PLL. Henceforth, we use the shorthand notation in (5).

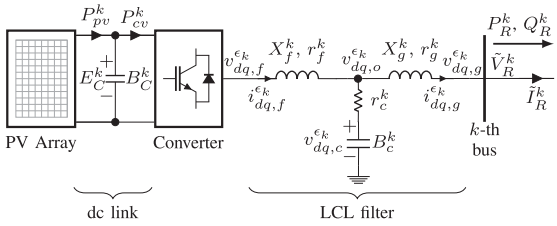

Fig. 1. Aggregated representation of a PV power plant.

[1]Here dq-axis notation differs from [3] (physical models do not) because of the particular choice of reference frame transformation, q.v. (4) for $\nu = r_n$.

[2]The dc exciter saturation model is accounted because it depends on one function only in contrast to the saturation model of ac synchronous machines that can depend on a number of saturation functions [3, p. 110].

[3]These models are used to simplify exposition; for detailed ones see [37].

A. Phase-Locked Loop

The dynamics of the k-th PLL are [8, p. 79], [29], [32]:

$$\frac{d}{dt}z_{\epsilon_k} = \frac{\kappa_\epsilon^k}{\tau_\epsilon^k}v_{q,g}^{\epsilon_k}, \quad \frac{d}{dt}\delta_{\epsilon_k} = \omega_b\left(\omega_{\epsilon_k} - \omega_e\right), \tag{24}$$

$$\omega_{\epsilon_k} = 1 + \kappa_\epsilon^k v_{q,g}^{\epsilon_k} + z_{\epsilon_k}\,. \tag{25}$$

The PLL variables include an integral compensator, z_{ϵ_k}, relative angle, δ_{ϵ_k}, and speed, ω_{ϵ_k}. The speed $d\delta_{\epsilon_k}/dt$ in (24) is obtained by referring $d\theta_{\epsilon_k}/dt = \omega_b\,\omega_{\epsilon_k}$ with respect to $d\theta_e/dt$ in (12). Note that the PLL model (24)–(25), which resides in a digital controller, reflects actual implementation [32] and is driven by: (i) the q-axis voltage, $v_{q,g}^{\epsilon_k}$, which is extracted from the voltage phasor $\tilde{V}_R^k$ [q.v. (53)], and (ii) the speed of the 'e' reference frame, $d\theta_e/dt$, in (12), which is also speed of $\tilde{V}_R^k$.

When a fault occurs, $\tilde{V}_R^k$ exhibits fast changes in magnitude and phase angle, hence $v_{q,g}^{\epsilon_k}$ has corresponding variations. This means that the PLL speed in (25) is sensitive to voltage transients (the impact of the actual grid speed could be minor).

B. Power Converter and Control

We neglect semiconductor switching dynamics as not being relevant to the transients of interest and instead consider terminal voltages averaged over a sliding window with length equal to the switching period, $T_{\rm sw}$. The averaged ac-side converter terminal voltages are denoted with $v_{dq,f}^{\epsilon_k}$. Using established pulse width modulation methods, the switch-cycle-averaged voltages can be engineered to track the control commands, $v_{dq,f}^{*k}$, when they are physically feasible [13]. In particular, the range of realizable converter ac voltage magnitude, $V_f^{*k} > 0$, is upper-bounded by the dc-link voltage, $v_C^k > 0$, hence the dq-axis converter voltages are modeled as:

$$v_{dq,f}^{\epsilon_k} = \left(\frac{\min\{V_f^{*k}, v_C^k\}}{V_f^{*k}}\right) v_{dq,f}^{*k} \tag{26}$$

$$V_f^{*k} = \sqrt{(v_{q,f}^{*k})^2 + (v_{d,f}^{*k})^2}\,. \tag{27}$$

Note that $v_{dq,f}^{\epsilon_k} = v_{dq,f}^{*k}$ if $v_C^k > V_f^{*k}$ as $\min\{V_f^{*k}, v_C^k\} = V_f^{*k}$, i.e., v_C^k is sufficient to realize $v_{dq,f}^{*k}$. Otherwise, the converter voltages will be limited by the available v_C^k. In Section IV-C, the per unit capacitor energy, $E_C^k = (v_C^k)^2$ (shown in Fig. 1), is modeled as a state for control purposes [13].

The dq-axis voltage commands are modeled with:

$$v_{dq,f}^{*k} = \kappa_i^k w_{dq,f}^k + z_{dq,f}^k - \omega_{\epsilon_k} X_f^k i_{qd,f}^{\epsilon_k} + v_{dq,o}^{\epsilon_k} \tag{28}$$

which contains a proportional-integral compensator and feed-forward voltages to regulate converter currents, $i_{dq,f}^{\epsilon_k}$. The controller errors, $w_{dq,f}^k$, and integral state, $z_{dq,f}^k$, of (28) are:

$$w_{dq,f}^k = i_{dq,f}^{*k} - i_{dq,f}^{\epsilon_k}, \text{ and } \frac{d}{dt}z_{dq,f}^k = \frac{\kappa_i^k}{\tau_i^k}w_{dq,f}^k \tag{29}$$

where $i_{dq,f}^{*k}$ are dq-axis current commands, q.v. Section IV-D.

Dynamics of the k-th converter-side inductor are:

$$\frac{d}{dt}i_{dq,f}^{\epsilon_k} = \frac{\omega_b}{X_f^k}\left(-r_f^k i_{dq,f}^{\epsilon_k} + \omega_{\epsilon_k} X_f^k i_{qd,f}^{\epsilon_k} + v_{dq,f}^{\epsilon_k} - v_{dq,o}^{\epsilon_k}\right) \tag{30}$$

$$v_{dq,o}^{\epsilon_k} = v_{dq,c}^{\epsilon_k} + r_c^k\left(i_{dq,f}^{\epsilon_k} - i_{dq,g}^{\epsilon_k}\right) \tag{31}$$

whereas the k-th ac capacitor dynamics are:

$$\frac{d}{dt}v_{dq,c}^{\epsilon_k} = \frac{\omega_b}{B_c^k}\left(\omega_\epsilon^k B_c^k v_{qd,c}^{\epsilon_k} + i_{dq,f}^{\epsilon_k} - i_{dq,g}^{\epsilon_k}\right). \tag{32}$$

As the PV power plant is integrated into a positive-sequence transmission grid (q.v. Section V), the k-th grid-side inductor is modeled in quasi-steady state, i.e.:[4]

$$0 = \frac{\omega_b}{X_g^k}\left(-r_g^k i_{dq,g}^{\epsilon_k} + X_g^k i_{qd,g}^{\epsilon_k} + v_{dq,o}^{\epsilon_k} - v_{dq,g}^{\epsilon_k}\right). \tag{33}$$

C. DC-Link and PV Array

The dc capacitor energy, $E_C^k = (v_C^k)^2$ of Fig. 1, satisfies:

$$\frac{d}{dt}E_C^k = \frac{1}{B_C^k}\left(P_{pv}^k - P_{cv}^k\right)\,. \tag{34}$$

This normalized model is derived from the rated line-to-line voltage base of the k-th converter, $\sqrt{2}V_{\rm nom}^k$, and volt-ampere base, S_b. Neglecting converter losses, the dc-side converter power is:

$$P_{cv}^k = v_{d,f}^{\epsilon_k} i_{d,f}^{\epsilon_k} + v_{q,f}^{\epsilon_k} i_{q,f}^{\epsilon_k}\,. \tag{35}$$

The PV array dc power, P_{pv}^k, and E_C^k are implicitly related, i.e., $\Phi^k(P_{pv}^k, E_C^k) = 0$, where $\Phi^k(\cdot,\cdot)$ derives from the PV array single-diode model [38]. As E_C^k is a state, P_{pv}^k satisfying $\Phi^k(\cdot,\cdot) = 0$ is solved numerically which is explained next.

The k-th PV array contains N_p^k parallel PV strings. Each string has N_s^k series-connected PV modules. The voltage:

$$v_m^k = \frac{\sqrt{2}V_{\rm nom}^k}{N_s^k}\sqrt{E_C^k} \tag{36}$$

and current, i_m^k, of all modules are assumed to be equal. This corresponds to uniform irradiance and temperature across the entire PV array [39]. The voltage (36) is mapped from the per unit dc-link energy, the number of series-connected modules, and the dc-link voltage base, $\sqrt{2}V_{\rm nom}^k$.

The circuit model for each PV module contains a current source whose magnitude, i_g^k, is proportional to irradiance [38]. The current through the module's internal diode, i_d^k, satisfies:

$$i_d^k = i_0^k\left(\mathsf{e}^{v_d^k/v_T^k} - 1\right) \text{ for } v_d^k = K_1^k - K_2^k i_d^k \tag{37}$$

where $i_0^k > 0$ is the diode reverse saturation current, v_d^k is the diode voltage, and:[5]

$$K_1^k = \frac{R_{sh}^k\left(v_m^k + R_s^k i_g^k\right)}{R_s^k + R_{sh}^k} \geq 0, \quad K_2^k = \frac{R_s^k R_{sh}^k}{R_s^k + R_{sh}^k} > 0\,. \tag{38}$$

[4]This expression can also represent an isolation transformer [8], [16].

[5]For physically feasible operation of PV arrays, $v_m^k \geq 0$ and $i_g^k \geq 0$.

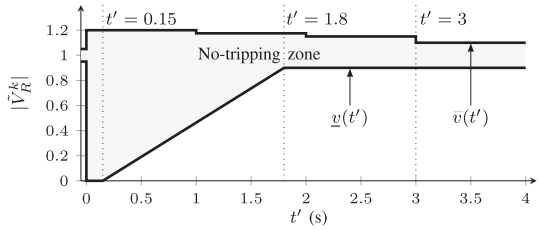

Fig. 2. WECC voltage ride-through envelope.

The voltage $v_T^k = \eta^k \frac{\kappa_B}{q_e} T^k N_c^k > 0$ depends on a nonideal factor, η^k; the Boltzmann constant, $\kappa_B = 1.3806 \times 10^{-23}$ J/K; the electron charge, $q_e = 1.6022 \times 10^{-19}$ C; the PV cell temperature T^k in Kelvin; and the number of series-connected PV cells within a module, N_c^k [38]. The resistances R_{sh}^k and R_s^k capture equivalent shunt and series resistances of the PV module. An i_d^k satisfying (37) and v_m^k of (36) yields:

$$i_m^k = \frac{K_1^k - K_2^k i_d^k - v_m^k}{R_s^k} \text{ and } P_{pv}^k = \frac{N_p^k N_s^k}{S_b} i_m^k v_m^k \,. \tag{39}$$

Various numerical methods are available to solve (37) [38]. One approach consists in creating a lookup table with solutions of (37) for a predetermined domain; however, *a priori* determination of dc-link energy extrema during faults is cumbersome. To avoid this problem, we employ a technique to find the zero (at each simulation step) of $g : \mathbb{R} \mapsto \mathbb{R}$ such that:

$$g(i_d^k) = i_0^k \left(\mathsf{e}^{(K_1^k - K_2^k i_d^k)/v_T} - 1 \right) - i_d^k \tag{40}$$

using (37) and fixed-point iterations (Newton's method) [34]:

$$i_{d,s+1}^k = i_{d,s}^k - \frac{g(i_{d,s}^k)}{g'(i_{d,s}^k)} \tag{41}$$

where $g'(i_d^k) = -1 - i_0^k \cdot \frac{K_2^k}{v_T^k} \mathsf{e}^{(K_1^k - K_2^k i_d^k)/v_T^k}$ for $s = 0, 1, \ldots$ and starting from $i_{d,0}^k = 0$. For sound numerical implementation, we prove convergence of (41) to a unique zero, regardless of the starting point $i_{d,0}^k$.

Lemma 1: The iterations in (41) with $g : \mathbb{R} \mapsto \mathbb{R}$ defined by (40) converges from any starting point $i_{d,0}^k$ to a unique zero $i_d^k = i_{d,c}^k$, which satisfies (37).

Proof: The function (40) has at least one zero crossing because $\lim_{i_d^k \to -\infty} g(i_d^k) > 0$ and $\lim_{i_d^k \to +\infty} g(i_d^k) < 0$. As $g'(i_d^k) < 0$ on $\mathbb{R}$; hence, $g(i_d^k)$ of (40) is always decreasing, which implies uniqueness of the zero, $i_{d,c}^k$. The decreasing monotonicity and convexity of (40) imply that the iterations in (41) converge to $i_{d,c}^k$ regardless of $i_{d,0}^k$, q.v. [34, p. 86]. ■

D. Current Commands for Faulted and Normal Operation

VRT codes mandate converter-based generation to remain connected as long as their terminal voltage (e.g., $\tilde{V}_R^k$ in Fig. 1) magnitudes remain within the envelope shown in Fig. 2 [31], [40]–[42]. Codes for distributed energy resources, e.g., IEEE 1547 [43], do not apply here because generation is connected to a bulk transmission system [8, p. 44]. The VRT envelope is typically defined by lower and upper time-domain bounds $\underline{v}(t')$ and $\overline{v}(t')$ [31], [44], where $t' = t - t_f$ is relative time with respect to that $t = t_f$ at which faulted voltages are observed by a converter. The codes also stipulate that converters shall inject zero active and some reactive current, I_{VRT}^{*k} (prescribed by a system operator [31], [44]), while the fault remains active, i.e., $t' \in [0, 0.15)$ s. After a fault is cleared ($t' \geq 0.15$ s), currents can be ramped to approach prefault values until control is switched back to normal at $t' = 1.8$ s.

Hence, the current commands in (29) are: [44]

$$i_{d,g}^{*k} = \begin{cases} 0 & \text{if } t' \in [0, 0.15] \text{ s} \\ \frac{t'-0.15}{1.65} \frac{i_E^{*k}(0^-)}{1.2} & \text{if } t' \in (0.15, 1.8] \text{ s} \\ i_E^{*k} & \text{if } t' \in (-\infty, 0) \cup (1.8, +\infty) \text{ s} \end{cases} \tag{42}$$

$$i_{q,g}^{*k} = \begin{cases} I_{\text{VRT}}^{*k} & \text{if } t' \in [0, 0.15] \text{ s} \\ \frac{1.8-t'}{1.65} I_{\text{VRT}}^{*k} \cdots & \\ + \frac{t'-0.15}{1.65} \frac{i_Q^{*k}(0^-)}{1.2} & \text{if } t' \in (0.15.1.8] \text{ s} \\ i_Q^{*k} & \text{if } t' \in (-\infty, 0) \cup (1.8, +\infty) \text{ s} \end{cases} \tag{43}$$

for VRT and normal operation. The VRT mode is activated at $t' = 0$ s (when voltages drop below 0.9 p.u.) and remains active until $t' = 1.8$ s (until voltages are expected to have recovered). During normal mode, the current commands i_E^{*k} and i_Q^{*k} regulate the dc-link capacitor voltage and PV power plant reactive power, respectively.

The dc-link voltage controller takes the form:[6]

$$w_E^k = E_C^{*k} - E_C^k \,, \; \frac{d}{dt} z_E^k = \frac{\kappa_E^k}{\tau_E^k} w_E^k \tag{44}$$

$$i_E^{*k} = -\kappa_E^k w_E^k - z_E^k. \tag{45}$$

so that E_C^k (34) tracks the MPPT-generated commands E_C^{*k}. Similarly, reactive power regulation is performed via:

$$w_Q^k = Q_R^{*k} - Q_R^k \,, \; \frac{d}{dt} z_Q^k = \frac{\kappa_Q^k}{\tau_Q^k} w_Q^k, \tag{46}$$

$$i_Q^{*k} = \kappa_Q^k w_Q^k + z_Q^k, \tag{47}$$

where Q_R^{*k} is dispatched by a grid operator and:

$$Q_R^k = v_{q,g}^{\epsilon_k} i_{d,g}^{\epsilon_k} - v_{d,g}^{\epsilon_k} i_{q,g}^{\epsilon_k} \tag{48}$$

is the reactive power at the PV power plant terminals.

V. Multi-Machine Multi-Converter Systems

Voltages and currents at any power plant terminals and within the transmission grid are assumed quasi-steady-state sinusoids cycling at $d\theta_e/dt$ in (12), hence modeled as phasors.

[6]Recall that the dc-link voltage is expressed in terms of energy, q.v. (34).

A. Dynamic Voltages Behind Impedances

The dynamic response of the n-th power plant of Section III can be viewed as a dynamic voltage source behind a transient impedance from the bulk transmission system [3, p. 100]:

$$\tilde{V}_C^n = -(r_s^n + \mathsf{j}X_d'^n)\tilde{I}_C^n + \tilde{E}_C^n, \tag{49}$$

$$\tilde{V}_C^n = \mathsf{e}^{\mathsf{j}\delta_{r_n}}\left(v_d^{r_n} + \mathsf{j}v_q^{r_n}\right),\ \tilde{I}_C^n = \mathsf{e}^{\mathsf{j}\delta_{r_n}}\left(i_d^{r_n} + \mathsf{j}i_q^{r_n}\right), \tag{50}$$

$$\tilde{E}_C^n = \mathsf{e}^{\mathsf{j}\delta_{r_n}}\left(e_d^{r_n} + \mathsf{j}e_q^{r_n}\right) \tag{51}$$

where the phasors $\tilde{V}_C^n$, $\tilde{I}_C^n$, and $\tilde{E}_C^n$ model the terminal voltage, terminal current, and dynamic voltage behind a transient impedance, respectively. The voltages $v_q^{r_n}$ and $v_d^{r_n}$ are from (20) and (21), respectively. The dynamics of $e_d^{r_n}$, $e_q^{r_n}$, and δ_{r_n} are modeled in (8), (9), and (11), respectively. The currents $i_d^{r_n}$ and $i_q^{r_n}$ for (8) and (9) are calculated in Section V-B.

Similarly, the response of a k-th PV power plant can be observed as a dynamic voltage source behind an impedance.

Proposition 1: Let the k-th PV power plant *dq* voltages:

$$e_{dq,g}^{\epsilon_k} := r_c^k i_{dq,f}^{\epsilon_k} + v_{dq,c}^{\epsilon_k}, \tag{52}$$

with $i_{dq,f}^{\epsilon_k}$ and $v_{dq,c}^{\epsilon_k}$ from (30) and (32). A dynamic voltage behind-impedance phasor of a k-th PV power plant is:

$$\tilde{V}_R^k = -(r_g^k + r_c^k + \mathsf{j}X_g^k)\tilde{I}_R^k + \tilde{E}_R^k, \tag{53}$$

$$\tilde{V}_R^k = \mathsf{e}^{\mathsf{j}\delta_{\epsilon_k}}\left(v_{d,g}^{\epsilon_k} + \mathsf{j}v_{q,g}^{\epsilon_k}\right),\ \tilde{I}_R^k = \mathsf{e}^{\mathsf{j}\delta_{\epsilon_k}}\left(i_{d,g}^{\epsilon_k} + \mathsf{j}i_{q,g}^{\epsilon_k}\right), \tag{54}$$

$$\tilde{E}_R^k = \mathsf{e}^{\mathsf{j}\delta_{\epsilon_k}}\left(e_{d,g}^{\epsilon_k} + \mathsf{j}e_{q,g}^{\epsilon_k}\right). \tag{55}$$

where δ_{ϵ_k} is the PLL relative angle in (24); and $\tilde{V}_R^k$, $\tilde{I}_R^k$, and $\tilde{E}_R^k$ are the terminal voltage, terminal current, and voltage behind impedance phasors, respectively.

Proof: The filter branch voltage in (31) and quasi-steady-state grid-side inductor model in (33) yields:

$$v_{dq,g}^{\epsilon_k} = -(r_g^k + r_c^k)i_{dq,g}^{\epsilon_k} + X_g^k i_{qd,g}^{\epsilon_k} + r_c^k i_{dq,f}^{\epsilon_k} + v_{dq,c}^{\epsilon_k}. \tag{56}$$

Hence, (53) follows from (56) by applying (52) and transforming variables into the 'e' reference frame via (7). ■

B. Bulk Transmission System

The transmission grid comprises step-up transformers, lines, and loads. To simplify modeling exposition, loads are represented as constant impedances [3], [33]. Hence, currents injected by conventional and renewable power plants can be related to their terminal voltages by [33]:

$$\begin{bmatrix}\tilde{I}_C\\ \tilde{I}_R\end{bmatrix} = \begin{bmatrix}Y_{CC}^{\gamma} & Y_{CR}^{\gamma}\\ Y_{RC}^{\gamma} & Y_{RR}^{\gamma}\end{bmatrix}\begin{bmatrix}\tilde{V}_C\\ \tilde{V}_R\end{bmatrix}, \tag{57}$$

$$\tilde{F}_G = [\tilde{F}_G^1, \ldots, \tilde{F}_G^n, \ldots, \tilde{F}_G^N]^\top, \tag{58}$$

where $\tilde{F} \in \{\text{'}\tilde{V}\text{'}, \text{'}\tilde{I}\text{'}\}$ is either a phasor vector of the terminal voltages or currents, and $G \in \{\text{'}C\text{'}, \text{'}R\text{'}\}$ identifies conventional or renewable generation. The matrix blocks Y_{CC}^{γ}, Y_{CR}^{γ}, Y_{RC}^{γ}, and Y_{RR}^{γ} are partitions of the admittance network matrix $Y^{\gamma} \in \mathbb{C}^{(N+K)\times(N+K)}$. Three network matrices indexed by $\gamma = \{1, 2, 3\}$ [see (1)] are considered to capture transmission disturbances. Notice Y^{γ} is by applying a network reduction technique, e.g., Kron, as loads are constant impedances [33].

Substitution of (49) (for $n = 1, \ldots, N$) and (53) (for $k = 1, \ldots, K$) into (57) via (58) yields:

$$\begin{bmatrix}\tilde{I}_C\\ \tilde{I}_R\end{bmatrix} = \begin{bmatrix}Y_{CC}'^{\gamma} & Y_{CR}'^{\gamma}\\ Y_{RC}'^{\gamma} & Y_{RR}'^{\gamma}\end{bmatrix}\begin{bmatrix}\tilde{E}_C\\ \tilde{E}_R\end{bmatrix}. \tag{59}$$

Notice the block matrices of (59) are similar to those of (57) but incorporate the reactances in (49) and (53) in order to calculate generation currents from the dynamic voltage behind-reactance phasors, q.v. (51) and (55).

C. Multi-Machine Multi-Converter Dynamics

The dynamics in Sections III and IV are consolidated as in (1), (2) with state vector $x^\top = [x_C^\top, x_R^\top]$, input vector $u^\top = [u_C^\top, u_R^\top]$, and output vector $y^\top = [y_C^\top, y_R^\top]$. The vectors:

$$x_C^\top = [E_{qd}'^{r\top}, \omega_r^\top, \delta_r^\top, V_a^\top, R_f^\top, E_{fd}^\top, T_m^\top, P_v^\top] \in \mathbb{R}^{9N} \tag{60}$$

$$x_R^\top = [z_\epsilon^\top, \delta_\epsilon^\top, z_{qd,f}^\top, I_{qd,f}^{\epsilon\top}, V_{qd,c}^{\epsilon\top}, E_C^\top, z_E^\top, z_Q^\top] \in \mathbb{R}^{11K} \tag{61}$$

contain the states of conventional and PV power plants.[7] To illustrate by example, vector notation has been simplified as:

$$E_{qd}'^{r\top} = [e_d^{r_1}, e_q^{r_1}, \ldots, e_d^{r_n}, e_q^{r_n}, \ldots, e_d^{r_N}, e_q^{r_N}] \tag{62}$$

$$z_\epsilon^\top = [z_{\epsilon_1}, \ldots, z_{\epsilon_k}, \ldots, z_{\epsilon_K}]. \tag{63}$$

In particular, the ODEs for (60) are formed with (8)–(11), (13)–(15), (22), and (23) $\forall n$. The ODEs for (61) are assembled with (24), (29), (30), (32), (34), (44), and (46) $\forall k$. The algebraic variables, viz., machine currents, $i_{dq}^{r_n}$ [q.v. (8)–(9)], and converter currents, $i_{dq,g}^{\epsilon_k}$ [q.v. (33)], are mapped via (59) from the voltage-behind reactance representation in (51), $\forall n$, and (55), $\forall k$.[8] The power, P_{pv}^k, of (34) is also an algebraic variable and mapped numerically from E_C^k, q.v. (36)–(41) $\forall k$.

External commands to the conventional and PV plants are:

$$u_C^\top = [V^{*\top}, P_v^{*\top}] \in \mathbb{R}^{2N}, \tag{64}$$

$$u_R^\top = [I_{\text{VRT}}^{*\top}, Q_g^{*\top}, E_C^{*\top}] \in \mathbb{R}^{3K}. \tag{65}$$

The input vector (64) is from (18) and (23), $\forall n$, whereas the vector (65) is from (43), (44), and (46), $\forall k$.

We select the following outputs for assessment:

$$y_C^\top = [|\tilde{V}_C|^\top, \Delta\omega_r^\top] \in \mathbb{R}^{2N} \tag{66}$$

$$y_R^\top = [|\tilde{V}_R|^\top, |\tilde{I}_f|^\top, v_C^\top, i_{pv}^\top, i_{cv}^\top] \in \mathbb{R}^{5K}. \tag{67}$$

[7] Note the number of states is similar to model both types of power plants which is indicative of similar computational burden.

[8] When considering more sophisticated load models, the modeling contributions of this paper remain intact.

which are assembled with $\tilde{V}_C^k$ of (49), $\tilde{V}_R^k$ of (53) and:

$$\Delta\omega_{r_n} = \omega_{r_n} - \omega_e \tag{68}$$

$$|\tilde{I}_f^k| = \sqrt{\left(i_{d,f}^{\epsilon_k}\right)^2 + \left(i_{q,f}^{\epsilon_k}\right)^2} \tag{69}$$

$$v_C^k = \sqrt{E_C^k},\ i_{cv}^k = \frac{P_{cv}^k}{v_C^k},\ i_{pv}^k = \frac{P_{pv}^k}{v_C^k}. \tag{70}$$

Here, ω_{r_n}, ω_e, $i_{dq,f}^{\epsilon_k}$, E_C^k, P_{cv}^k, P_{pv}^k are from (10), (12), (30), (34), (35), (39), respectively. Note that i_{cv}^k and i_{pv}^k are currents measured at the converter and PV array dc terminals.

VI. Transient Stability Assessment

Numerical simulations of the power system dynamics, consolidated in Section V-C, are assessed in terms of multi-swing rotor angle stability as well as compliance of VRT codes while meeting voltage and current limits. The transient begins at $t = t_f$ because of a grid fault, which is cleared at $t = t_c$.

Definition 1: A rotor angle [δ_{r_n} of (11)] is said to 'swing' when it reaches a maximum or minimum in time [36].

Definition 2: Consider sequences of n-th relative rotor speeds $\{\Delta\omega_{r_n}(t_o)\}_{o=c}^{n_o}$ with $t_o \in [t_c, T]$. The rotor angle δ_{r_n} is first-swing stable if $\exists o$ such that [2, p. 44]:

$$\Delta\omega_{r_n}(t_o)\,\Delta\omega_{r_n}(t_{o+1}) < 0\,. \tag{71}$$

Further, the n-th rotor angle is exponentially stable, i.e., multi-swing stable [2, p. 61], if there exists positive constants λ_n and ρ_n, such that [45, p. 150]:

$$|\Delta\omega_{r_n}(t_o)| \le \rho_n |\Delta\omega_{r_n}(t_c)| \mathsf{e}^{-\lambda_n (t_o - t_c)} \tag{72}$$

for all $t_o \in [t_c, T]$.

Notice from (12) and (68) that if all rotors regain synchronism, the relative speeds $\Delta\omega_{r_n}$ for $n = 1, \ldots, N$ converge to the origin. We calculate λ_n and ρ_n of (72) as follows:

(1) Identify times t_ξ with $\xi = 1, 2, \ldots$ at which peaks of $\{|\Delta\omega_{r_n}(t_o)|\}_{o=c}^{n_o}$ occur. To this end, estimate the zeros of $\Delta\omega_{r_n}$ via (71), and find all $\max |\Delta\omega_{r_n}(t_o)|$ for $t_o \in (t_z, t_{z+1})$ with t_z, t_{z+1} consecutive zero crossings.

(2) Calculate the exponential λ_n by solving:

$$\min_{\lambda_n\,,\,\beta_n} \sum_{\xi} \left(\beta_n - \lambda_n (t_\xi - t_c) - \ln |\Delta\omega(t_\xi)|\right)^2 \tag{73}$$

obtained from $|\Delta\omega(t_\xi)| = \mathsf{e}^{r_\xi + \beta_n - \lambda_n (t_\xi - t_c)}$ to minimize the residuals r_ξ in a least-squares sense [46, p. 291].

(3) If $\lambda_n > 0$ in the previous step, calculate:

$$\rho_n = \max_{\xi} \left(\frac{|\Delta\omega_{r_n}(t_\xi)|}{|\Delta\omega_{r_n}(t_c)|\, \mathsf{e}^{-\lambda_n (t_\xi - t_c)}} \right). \tag{74}$$

Definition 3: The n-th synchronous generator complies with VRT codes for $t_o' = t_o - t_f$ if its terminal voltages satisfy:

$$|\tilde{V}_C^n(t_o')| \in [\underline{v}(t_o'), \overline{v}(t_o')] \tag{75}$$

with $\underline{v}(t')$ and $\overline{v}(t')$ defined by a VRT envelope, e.g., Fig. 2.

To asses PV power plants, converter rated currents and voltages are considered. Converter protection software might trip the converter only if rated physical limits are violated [8]. The PLL angle and speed are not assessed because they are software variables that do not imply converter damage. A feature of the assessment is that it considers dynamics that may lead to the disconnection of PV power plants, e.g., reverse dc-link current as well as ac and dc voltage transients [8].

Definition 4: Consider sequences of k-th PV power plant terminal voltage magnitudes $\{|\tilde{V}_R^k(t_o)|\}_{o=1}^{n_o}$, converter ac current $\{|\tilde{I}_f^k(t_o)|\}_{o=1}^{n_o}$, converter dc voltage $\{v_{dc}^k(t_o)\}_{o=1}^{n_o}$, converter dc current $\{i_{dc}^k(t_o)\}_{o=1}^{n_o}$, and PV array dc current $\{i_{pv}^k(t_o)\}_{o=1}^{n_o}$ with $t_o \in (0, T)$. The power plant performs satisfactorily if:

$$|\tilde{V}_R^k(t_o')| \in [\underline{v}(t_o'), \overline{v}(t_o')] \tag{76}$$

$$|\tilde{I}_f^k(t_o)| \in [0, I_f^k]\,,\ v_C^k(t_o) \in [\underline{v}_C^k, \overline{v}_C^k] \tag{77}$$

$$i_{cv}^k(t_o) \in [\underline{i}_{cv}^k, \overline{i}_{cv}^k]\,,\ i_{pv}^k(t_o) \in [\underline{i}_{pv}^k, \overline{i}_{pv}^k] \tag{78}$$

for all $t_o \in (0, T]$ and given: (i) VRT envelope, e.g., of Fig. 2; (ii) maximum converter current magnitude I_f^k; iii) dc-link voltage limits $\underline{v}_{dc}^k$ and $\overline{v}_{dc}^k$; iv) converter dc current bounds $\underline{i}_{cv}^k$ and $\overline{i}_{cv}^k$; and v) PV array dc current bounds $\underline{i}_{pv}^k$ and $\overline{i}_{pv}^k$. The ratings (77)–(78) are specified by a manufacturer, e.g., [47].

Definition 5: A multi-machine multi-converter power system simulation is stable and performs satisfactorily if each:

i) n-th conventional plant satisfies Definitions 2 and 3 and the
ii) k-th renewable plant satisfies Definition 4

for all $n = 1, \ldots, N$ and $k = 1, \ldots, K$.

VII. Case Studies

We simulate power system models as in (1), (2) which are consolidated in Section V-C. Then, they are assessed via the definitions of Section VI. In particular, we conduct two case studies of modified versions of the WSCC 9-bus as well as the IEEE 39-bus power systems, respectively. Integration of the developed PV model into *larger* power systems should be rather straightforward because the system representation of Section V-C is derived for arbitrary numbers of conventional and PV power plants, q.v. (60) and (61).

The numerical studies were performed on a 2.9-GHz Intel Core i7 personal computer running MATLAB R2018a [48]. The CPU time to execute 5- and 11-second simulations of the WSCC 9-bus and IEEE 39-bus power systems were 2.14 s and 3.53 s, respectively. The simulations trust in the ode15s solver available in MATLAB and are automatically assessed as explained in Section VI. Initial conditions are obtained by solving the power flow problem with MATPOWER and the calculations in [33, p. 392].[9] The considered system bases are $S_b = 100$ MVA and $\omega_b = 120\pi$ rad/s. In each case study, parameters of a k-th PV power plant with rating S_{nom}^k are obtained in the base S_b by defining $\beta^k := S_b / S_{\text{nom}}^k$ and scaling the values of Table I as

[9]The PV power plants are considered to be attached to 'PQ' buses. State initialization of converter-based and conventional generation is similar [33].

TABLE I
PARAMETERS OF PV ARRAY AND CONVERTER

Para.	Value	Unit	Para.	Value	Unit
r_f	0.0015	p.u.	X_f	0.15	p.u.
r_g	0.0012	p.u.	X_g	0.03	p.u.
r_c	0.4623	p.u.	B_c	0.0326	p.u.
κ_i	6.934	p.u.	τ_i	0.017	s
κ_E	0.0173	p.u.	τ_E	0.1	s
κ_Q	0.7205	p.u.	τ_Q	0.1	s
κ_ϵ	0.690	p.u.	τ_ϵ	0.125	s
B_C	8.653×10^{-4}	p.u.	i_0	7.1712×10^{-13}	A
R_s	0.5371	Ω	R_{sh}	419.78	Ω
η	0.87223	–	N_c	128	–

Converter switching period $T_{\text{sw}} = 1/3$ ms.

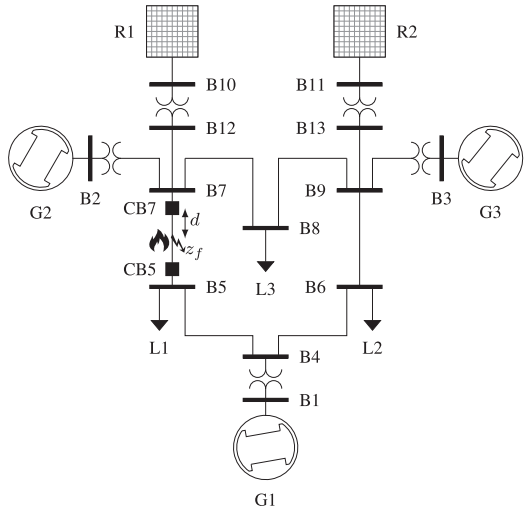

Fig. 3. Modified WSCC nine-bus power system.

TABLE II
RENEWABLE POWER PLANTS FOR CASE STUDY I

Para.	$k=1$	$k=2$	Units	Para.	$k=1$	$k=2$	Units
S^k_{nom}	50	50	MVA	V^k_{nom}	0.66	0.66	kV
P^k_R	30	40	MW	Q^k_R	-20	-20	MVAr
i^k_g	3.517	4.615	A	E^{*k}_C	1.651	1.655	p.u.
T^k	308	308	K	N^k_s	16	16	–
				N^k_p	7813	7813	–

Each k-th PV array is composed by 400-W_{dc} modules @ 72-V_{dc} ca.

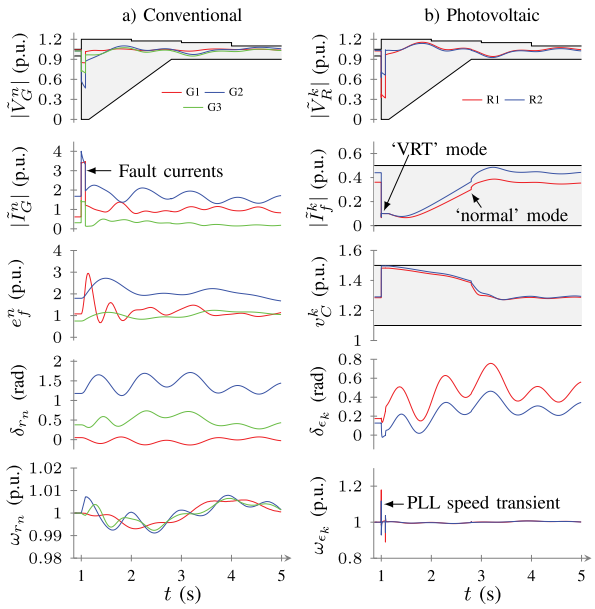

Fig. 4. Case I: Transient behavior of conventional and PV power plants during transmission disturbances. The gray areas bounded by solid-black envelopes indicate acceptable variable ranges.

follows [29]:

$$r_f^k = \beta^k r_f,\ r_g^k = \beta^k r_g,\ r_c^k = \beta^k r_c, \tag{79}$$

$$X_f^k = \beta^k X_f,\ X_g^k = \beta^k X_g,\ B_c^k = B_c/\beta^k, \tag{80}$$

$$\kappa_\epsilon^k = \kappa_\epsilon,\ \tau_\epsilon^k = \tau_\epsilon,\ \kappa_i^k = \beta^k \kappa_i,\ \tau_i^k = \tau_i,\ \kappa_Q^k = \kappa_Q, \tag{81}$$

$$B_C^k = B_C/\beta^k,\ \kappa_E^k = \beta^k \kappa_E,\ \tau_E^k = \tau_E,\ \tau_Q^k = \tau_Q, \tag{82}$$

$$i_0^k = i_0,\ \eta^k = \eta,\ N_c^k = N_c,\ R_{sh}^k = R_{sh},\ R_s^k = R_s\,. \tag{83}$$

A. Case Study I: Modified WSCC 9-Bus Power System

A modified version of the WSCC 9-bus power system is considered as being relatively simple to interpret [33, p. 37–39]. This system is illustrated in Fig. 3 which has thirteen buses; three conventional machines, G1, G2, G3 ($N = 3$); and two PV power plants, R1, R2 ($K = 2$). Machine G1 is driven by a hydro turbine, whereas G2 and G3 are driven by steam turbines. Parameters of the WSCC power system are in [33, p. 37–39], and the excitation system parameters are in [36], $\chi = 51$ in (17). Parameters of the transmission lines B10–B7 and B11–B9 are the same as for line B6–B9.[10] Each PV power plant has a rating $S^k_{\text{nom}} = 50$ MVA (for $k \in \{1, 2\}$) and interfaces to the grid via a step-up transformer with 4% impedance on the 50-MVA base. Generators G1, G2, and G3, supply 0.5944, 1.72, and 0.2 p.u. active power to the system, respectively. PV power plant operational conditions are specified in Table II.

We study the system response to a three-phase fault on line B5–B7. The simulation starts at $t = t_0 = 0$ and concludes at $t = T = 5$ s. The fault occurs at $t = t_f = 1$ s and is located at a distance $d = 0.324$ p.u. (referred to the total length of line B7–B5 and measured from B7). We consider a symmetrical fault impedance $z_f = (0.174 + j3.813) \times 10^{-3}$ p.u. [10, p. 19]. The fault is cleared by opening the circuit breakers CB5 and CB7 after 5 cycles of 60 Hz (i.e., $t_c = t_f + 5/60$ s). Both PV power plants are set to inject VRT current $I^{*k}_{\text{VRT}} = 0.1$ p.u. during the fault, q.v. (42) and (43). (Injection of high VRT currents was not necessary because voltage recovery was not problematic). Transient behavior of the power plants is depicted in Figs. 4–6.

Simulated performance of conventional generation is assessed via Definitions 2 and 3 and the variables shown in Figs. 4(a) and 5. As evident in Fig. 4(a), the generator voltages, $|\tilde{V}^n_C|$, do not violate the VRT envelope. Conventional generator currents, $|\tilde{I}^n_C|$, and excitation voltages, e^n_f, rise during the fault as expected. Relative rotor angles, δ_{r_n}, and speeds, ω_{r_n}, appear stable with a superficial inspection, but this is not conclusive of rotor angle stability. Hence, we apply Definition 2 to show

[10] A power line linking two buses, e.g., B6 and B9, is denoted by B6–B9.

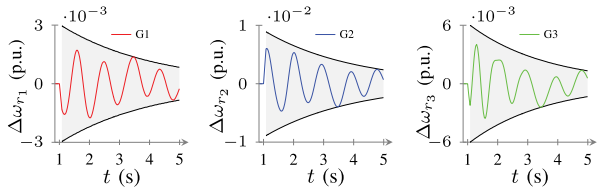

Fig. 5. Case I: Multi-swing rotor-angle stability assessment. The gray areas bounded by solid-black envelopes are used to assess rotor-angle stability.

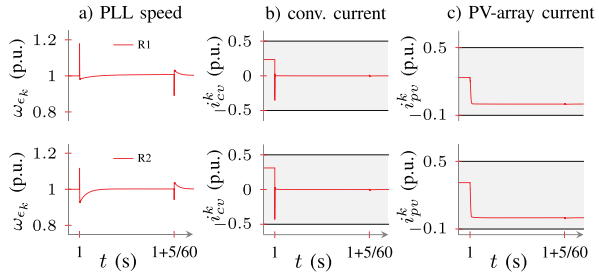

Fig. 6. Case I: Fast PV power plant transients during transmission disturbances. The gray areas bounded by solid-black envelopes illustrate rated limits of converter and PV-array dc currents.

in Fig. 5 that relative speed trajectories are indeed bounded by stable envelopes, which ascertains multi-swing stability. The tuples $(\lambda_n, \rho_n, |\Delta\omega_{r_n}(t_c)|)$ in (72) for each $n = 1, 2, 3$ that yield the envelopes of Fig. 5 are: (0.286,2.062,0.0013), (0.302,1.378,0.006), and (0.332,2.372,0.002), respectively.

PV power plant performance is analyzed via Definition 4 and corresponding traces in Figs. 4(b) and 6. Each PV power plant is deemed to have satisfactory performance if $|\tilde{V}_R^k|$ lies in the VRT envelope, $|\tilde{I}_f^k|(t) \in [0, 0.5]$ p.u., $v_C^k(t) \in [1.1, 1.5]$ p.u., $i_{cv}^k(t) \in [-0.5, 0.5]$ p.u., and $i_{pv}^k(t) \in [-0.1, 0.5]$ p.u. These limits are representative of manufacturer specifications for a 50-MVA PV power plant. In Fig. 4(b), we observe that $|\tilde{V}_R^k|$, $\tilde{I}_f^k(t)$, and $v_C^k(t)$ satisfy the established performance requirements. The ac currents, $|\tilde{I}_f^k(t)|$, track the VRT current commands during the fault, then ramp up until resuming normal operation at $t = 1.8$ s, q.v. (42), (43).

To further elucidate PV plant operation during network transients, the PLL speed and dc-link currents are depicted in Fig. 6. Because each PLL is driven by grid-terminal voltages, brief spikes are seen in Fig. 6(a) during network topology changes, i.e., at $t = t_f = 1$ s and $t = t_c = t_f + 5/60$ s [q.v. (24), (25)]. Because PLLs are executed digitally, off-nominal PLL speed is not indicative of converter damage. In Fig. 6(b), dc-side converter currents experience momentary reverse spikes because of the terminal voltage phase jumps. Conservatively designed converter protection might disconnect a PV plant during this current reversal because it might be falsely interpreted as a dc-link fault. This mirrors North American Electric Reliability Corporation reliability guidelines [8] which specify that protection settings should be configured to avoid unnecessary tripping. The zero currents in Fig. 6(c) are not problematic, albeit this is indicative that the PV array is dissipating power. Because this case study meets Definition 5, the simulated multi-machine multi-converter system is stable and performs satisfactorily.

TABLE III
RENEWABLE POWER PLANTS FOR CASE STUDY II

Para.	$k=1$	$k=2$	$k=3$	Units	Para.	$k=1$	$k=2$	$k=3$	Units
S^k_{nom}	700	700	700	MVA	V^k_{nom}	0.66	0.66	0.66	kV
P^k_R	508	650	560	MW	Q^k_R	165.8	212.4	101.2	MVAr
i^k_q	4.205	5.322	4.612	A	E^{*k}_C	1.661	1.670	1.666	p.u.
T^k	308	308	308	K	N^k_s	16	16	16	–
					N^k_p	110k	110k	110k	–

Each k-th PV array is composed by 400-W_{dc} modules @ 72 V_{dc} ca.

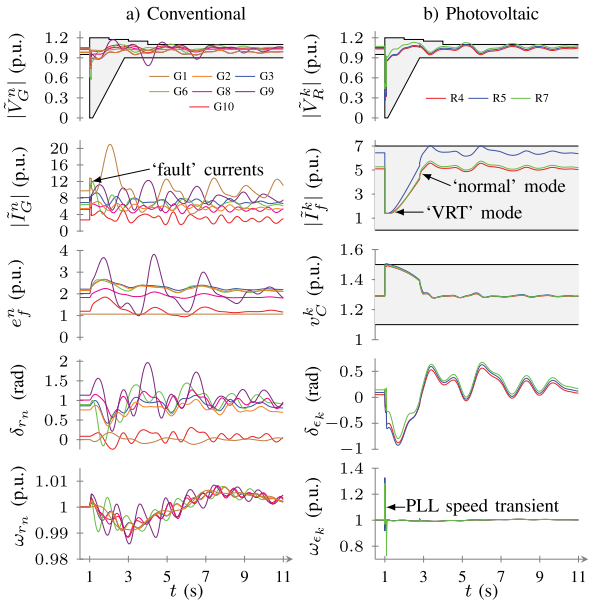

Fig. 7. Case II: Transient behavior of conventional and PV power plants during transmission disturbances. The gray areas bounded by solid-black envelopes indicate acceptable variable ranges.

B. Case Study II: Modified IEEE 39-Bus Power System

The IEEE 39-bus power system is considered here because it exhibits nonlinear dynamics that are representative of large power systems. This system, detailed in [49], has ten power plants, viz., one representing an interconnection G1; eight steam G2–G9; and one hydro G10. The modified system results after substitution of the units G4, G5, and G7 (connected to buses B33, B34, and B36) by three PV power plants R4, R5, and R7, respectively. The resulting multi-machine multi-converter power system has, $N = 7$, conventional units and, $K = 3$, PV power plants. Parameters for the machines and excitation systems of the conventional generation are specified in [50, p. 226]. The rating of each PV power plant and their pre-fault operational conditions are specified in Table III.

We consider a symmetrical fault with impedance z_f and distance d as for Case Study I. The simulation starts at $t = t_0 = 0$ and concludes at $t = T = 11$ s. The fault occurs at $t = t_f = 1$ s, is cleared at $t = t_c = t_f + 5/60$ s, and is located within line B17–B16 with d measured from B17 (please refer to [49, Fig. 1]). The VRT current of each PV power plant $I^{*k}_{\text{VRT}} = 1.4$ p.u. The transient performance of the modified IEEE 39-bus power system is illustrated in Figs. 7–9.

Fig. 7 shows that time-domain voltages $|\tilde{V}^n_G|$ and $|\tilde{V}^k_R|$ violate the VRT envelope (even during pretransient). This is particularly

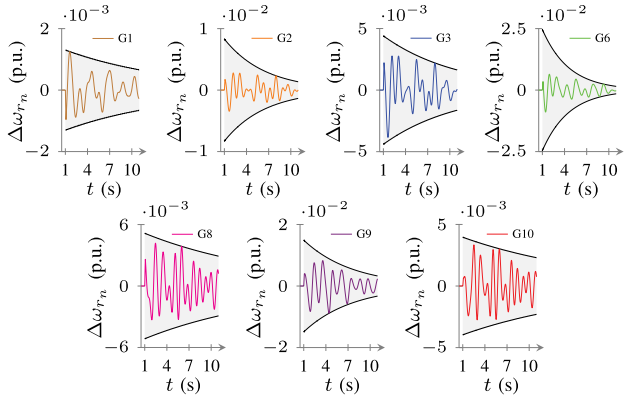

Fig. 8. Case II: Multi-swing rotor-angle stability assessment. The gray areas bounded by solid-black envelopes are used to assess rotor-angle stability.

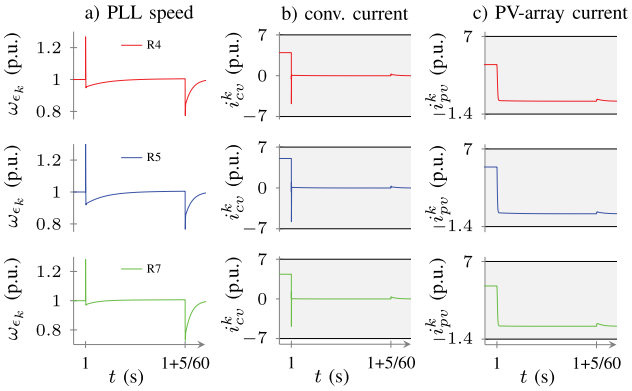

Fig. 9. Case II: Fast PV power plant transients during transmission disturbances. The gray areas bounded by solid-black envelopes illustrate rated limits of converter and PV-array dc currents.

problematic for PV power plants R5 and R7 because they *may* disconnect. Also, the dc-link voltage v_C^k of R5 slightly exceeds its rated limits which could trigger converter-level protection. The relatively high current $\tilde{I}_G^n$ corresponding to G1 after clearing the fault is caused by the momentarily but significant loss of PV power as result of VRT mode. In Fig. 8, the relative-rotor speeds are bounded by stable envelopes which imply that the machines will reach synchrony. Fig. 9 shows that reverse converter dc currents occur which could trigger internal converter protection if conservative settings are used. Although the system is stable, it does not perform well because of ac and dc voltage violations, q.v. Definitions 3–5. For this admittedly hypothetical system, engineers would likely need to rectify the identified problems.

VIII. Conclusion

A PV power plant model considering a PLL, ac- and dc-side dynamics, and closed-loop controllers has been proposed. The model is compatible with positive-sequence bulk power system models because of the developed voltage-behind-reactance representation. To assess the transient stability of multi-machine multi-converter power systems from simulations, a set of stability and performance metrics has been introduced. The illustrated case studies show that off-nominal PLL speed and reverse dc-link current might be manifested as a result of ac voltage transients. This aligns with observations in reliability guidelines regarding PLL and dc-link behavior [8].

The proposed framework can be tailored to study any PV converter control strategy of interest and used to predict system behavior during faults. Remarkably, this can be achieved without resorting on EMT studies that are typically computationally expensive [17], albeit assessment from EMT and positive-sequence simulations may yield differences and deserve further study. The contributions of this paper might be also appropriate to study other renewable generation assets, e.g., Type-3 and -4 wind turbines. Also, to model converter-based technologies that store/release energy such as variable speed pump/turbine stations, flywheels, compressed air, and batteries [27], [51]. Further, the paper could be relevant to study the response of PV power plants as a distributed energy resource and supplying a variety of power system load components that may have adverse impacts. These topics were not undertaken here, but could represent a research direction.

Acknowledgment

The views expressed in the article do not necessarily represent the views of the DOE or the U.S. Government. The U.S. Government retains and the publisher, by accepting the article for publication, acknowledges that the U.S. Government retains a nonexclusive, paid-up, irrevocable, worldwide license to publish or reproduce the published form of this work, or allow others to do so, for U.S. Government purposes.

References

[1] C. P. Steinmetz, "Power control and stability of electric generating stations," *Trans. Amer. Inst. Elect. Eng.*, vol. XXXIX, no. 2, pp. 1215–1287, Jul. 1920.

[2] M. Pavella, D. Ernst, and D. Ruiz-Vega, *Transient Stability of Power Systems: A Unified Approach to Assessment and Control*. Norwell, MA, USA: Kluwer, 2000.

[3] P. W. Sauer and M. A. Pai, *Power System Dynamics and Stability*. Champaign, IL, USA: Stipes, 2006.

[4] IEEE Committee, "Computer representation of excitation systems," *IEEE Trans. Power App. Syst.*, vol. PAS-87, no. 6, pp. 1460–1464, Jun. 1968.

[5] S. Jin *et al.*, "Comparative implementation of high performance computing for power system dynamic simulations," *IEEE Trans. Smart Grid*, vol. 8, no. 3, pp. 1387–1395, May 2017.

[6] R. Domínguez, A. J. Conejo, and M. Carrión, "Toward fully renewable electric energy systems," *IEEE Trans. Power Syst.*, vol. 30, no. 1, pp. 316–326, Jan. 2015.

[7] B. Kroposki *et al.*, "Achieving a 100% renewable grid: Operating electric power systems with extremely high levels of variable renewable energy," *IEEE Power Energy Mag.*, vol. 15, no. 2, pp. 61–73, Mar./Apr. 2017.

[8] NERC, "Reliability guideline: BPS-connected inverter-based resource performance," North Amer. Electr. Rel. Corp., Atlanta, GA, USA, Tech. Rep., Sep. 2018.

[9] AEMO, "Black system south Australia: 28 September 2016," Australian Energy Market Operator Ltd., Sydney, Australia, Tech. Rep., Mar. 2017.

[10] NERC/WECC Inverter Task Force, "1200 MW fault induced solar photovoltaic resource interruption disturbance report: Southern California 8/16/2016 event," North Amer. Electr. Rel. Corp., Atlanta, GA, USA, Tech. Rep., Jun. 2017.

[11] NERC/WECC, "900 MW fault induced solar photovoltaic resource interruption disturbance," North Amer. Electr. Rel. Corp., Atlanta, GA, Tech. Rep., Feb. 2018.

[12] H. Nikkhajoei and R. Iravani, "Dynamic model and control of AC–DC–AC voltage-sourced converter system for distributed resources," *IEEE Trans. Power Del.*, vol. 22, no. 2, pp. 1169–1178, Apr. 2007.

[13] A. Yazdani and R. Iravani, *Voltage-Sourced Converters in Power Systems: Modeling Control and Applications*. Hoboken, NJ, USA: Wiley, 2010.
[14] P. C. Krause, O. Wasynczuk, S. D. Sudhoff, and S. Pekarek, *Analysis of Electric Machinery and Drive Systems*, 3rd ed. New York, NY, USA: IEEE Press/Wiley-Interscience, 2013.
[15] X. Zhao *et al.*, "Low-voltage ride-through operation of power converters in grid-interactive microgrids by using negative-sequence droop control," *IEEE Trans. Power Electron.*, vol. 32, no. 4, pp. 3128–3142, Apr. 2017.
[16] WECC Renewable Energy Modeling Task Force, *WECC PV Power Plant Dynamic Modeling Guide*. Salt Lake City, UT, USA: Western Electricity Coordinating Council, Apr. 2014.
[17] S. Abourida *et al.*, "Real-time power system simulation: EMT vs. phasor," OPAL-RT Technol., Montreal, QC, Canada, White Paper opWP150620-sa-revA, 2016.
[18] WECC Renewable Energy Modeling Task Force, *WECC Wind Plant Dynamic Modeling Guidelines*. Salt Lake City, UT, USA: Western Electricity Coordinating Council, May 2014.
[19] J. Fortmann *et al.*, "New generic model of DFG-based wind turbines for RMS-type simulation," *IEEE Trans. Energy Convers.*, vol. 29, no. 1, pp. 110–118, Mar. 2014.
[20] *Wind Turbines—Part 27-1: Electrical Simulation Models—Wind Turbines*, IEC Standard 61 400-27-1, Rev. 1.0, Feb. 2015.
[21] A. Honrubia-Escribano *et al.*, "Field validation of a standard type 3 wind turbine model for power system stability, according to the requirements imposed by IEC 61400-27-1," *IEEE Trans. Energy Convers.*, vol. 33, no. 1, pp. 137–145, Mar. 2018.
[22] E. Vittal, M. O'Malley, and A. Keane, "Rotor angle stability with high penetrations of wind generation," *IEEE Trans. Power Syst.*, vol. 27, no. 1, pp. 353–362, Feb. 2012.
[23] E. Vittal, A. Keane, J. G. Slootweg, and W. Kling, "Impacts of wind power on power system stability," in *Wind Power in Power Systems*. Chichester, U.K.: Wiley, 2012, pp. 891–912.
[24] P. N. Papadopoulos and J. V. Milanović, "Probabilistic framework for transient stability assessment of power systems with high penetration of renewable generation," *IEEE Trans. Power Syst.*, vol. 32, no. 4, pp. 3078–3088, Jul. 2017.
[25] T. Sadamoto *et al.*, "Retrofit control of wind-integrated power systems," *IEEE Trans. Power Syst.*, vol. 33, no. 3, pp. 2804–2815, May 2018.
[26] M. Altin, Ö. Göksu, P. Sørensen, A. Morales, J. Fortmann, and F. J. Buendia, "Phase angle calculation dynamics of type-4 wind turbines in rms simulations during severe voltage dips," *IET Renew. Power Gen.*, vol. 10, no. 8, pp. 1069–1186, Sep. 2016.
[27] Á. Ortega and F. Milano, "Generalized model of VSC-based energy storage systems for transient stability analysis," *IEEE Trans. Power Syst.*, vol. 31, no. 5, pp. 3369–3380, Sep. 2016.
[28] Á. Ortega and F. Milano, "Frequency control of distributed energy resources in distribution networks," in *Proc 10th Symp. Control Power Energy Syst.*, Tokyo, Japan, Sep. 2018, pp. 37–42.
[29] V. Purba *et al.*, "Reduced-order structure-preserving model for parallel-connected three-phase grid-tied inverters," in *Proc. IEEE 18th Workshop Control Model. Power Electron.*, Stanford, CA, USA, Jul. 9–12, 2017, pp. 1–7.
[30] P. Kundur, *Power System Stability and Control* (ser. The EPRI Power System Engineering), N. J. Balu and M. G. Lauby, Eds. Palo Alto, CA, USA: McGraw-Hill, 1994.
[31] Wind Generation Task Force, "The technical basis for the new WECC voltage ride-through (VRT) standard," Western Electricity Coordinating Council, Salt Lake City, UT, USA, Tech. Rep., Jun. 2007.
[32] S. Golestan, J. M. Guerrero, and J. C. Vasquez, "Three-phase PLLs: A review of recent advances," *IEEE Trans. Power Electron.*, vol. 32, no. 3, pp. 1894–1907, Mar. 2017.
[33] P. M. Anderson and A. A. Fouad, *Power System Control and Stability* (IEEE Press Power Engineering Series), 2nd ed. New York, NY, USA: Wiley, 2003.
[34] D. Kincaid and W. Cheney, *Numerical Analysis: Mathematics of Scientific Computing*, 3rd ed. Pacific Grove, CA, USA: Brooks/Cole, 2002.
[35] W. Gautschi, *Numerical Analysis*, 2nd ed. New York, NY, USA: Birkhäuser, 2012.
[36] H. N. Villegas Pico, D. C. Aliprantis, and X. Lin, "Transient stability assessment of power systems with uncertain renewable generation," in *Proc. 10th Bulk Power Syst. Dyn. Control Symp.*, Espinho, Portugal, Aug. 27–Sep. 1, 2017, [Online]. Available: http://irep2017.inesctec.pt/conference-papers/conference-papers/paper81f1i1qsst.pdf
[37] IEEE Power and Energy Society, "Dynamic models for turbine-governors in power system studies," IEEE Power Energy Soc., Piscataway, NJ, USA, Tech. Rep. PES-TR1, Jan. 2013.
[38] M. G. Villalva, J. R. Gazoli, and E. R. Filho, "Comprehensive approach to modeling and simulation of photovoltaic arrays," *IEEE Trans. Power Electron.*, vol. 24, no. 5, pp. 1198–1208, May 2009.
[39] A. Hoke *et al.*, "Rapid active power control of photovoltaic systems for grid frequency support," *J. Emerg. Sel. Topics Power Electron.*, vol. 5, no. 3, pp. 1154–1163, Sep. 2017.
[40] "Interconnection for wind energy," Federal Energy Regulatory Commission, FERC Order 661-A, Dec. 2005. [Online]. Available: https://www.ferc.gov/CalendarFiles/20051212171744-RM05-4-001.pdf
[41] M. Tsili and S. Papathanassiou, "A review of grid code technical requirements for wind farms," *IET Renew. Power Gener.*, vol. 3, no. 3, pp. 308–332, Sep. 2009.
[42] *Reactive Power Requirements for Non-Synchronous Generation*, Federal Energy Regulatory Commission Standard Order No. 827, Docket No. RM16-1-000, Jun. 2016.
[43] Standards Coordinating Committee 21, *IEEE Standard for Interconnection and Interoperability of Distributed Energy Resources with Associated Electric Power Systems Interfaces*, IEEE Standard 1547-2018, Rev. IEEE Std 1547-2003, Apr. 2018.
[44] H. N. Villegas Pico and D. C. Aliprantis, "Voltage ride-through capability verification of wind turbines with fully-rated converters using reachability analysis," *IEEE Trans. Energy Convers.*, vol. 29, no. 2, pp. 392–405, Jun. 2014.
[45] H. K. Khalil, *Nonlinear Systems*, 3rd ed. Upper Saddle River, NJ, USA: Prentice-Hall, 2002.
[46] S. Boyd and L. Vandenberghe, *Convex Optimization*. Cambridge, U.K.: Cambridge Univ. Press, 2009.
[47] *Medium Voltage Power Station*, 1st ed., SMA Solar Technology AG, Niestetal, Germany, 2015. [Online]. Available: http://files.sma.de/dl/21337/MVPSCPXT-SH-en-13.pdf
[48] *MATLAB R2018a*, The MathWorks Inc. Natick, MA, USA, 2018. [Online]. Available: http://www.mathworks.com
[49] I. Hiskens, "39-bus system (New England Reduced Model)," IEEE PES Task Force on Benchmark Systems for Stability Controls, Tech. Rep., Nov. 2013.
[50] M. A. Pai, *Energy Function Analysis for Power System Stability* (ser. Power Electronics and Power Systems). New York, NY, USA: Springer, 1989.
[51] V. Koritarov *et al.*, "Modeling and analysis of value of advanced pumped storage hydropower in the United States," Argonne Nat. Lab., Lemont, IL, USA, Tech. Rep. ANL/DIS-14/7, Jun. 2014.

Hugo N. Villegas Pico (M'17) received the Degree of Ingeniero in electrónica, automatización y control from the Universidad de las Fuerzas Armadas, Sangolquí, Ecuador, in 2008, the M.S. degree in electrical engineering from Iowa State University, Ames, IA, USA, in 2011, and the Ph.D. degree in electrical and computer engineering from Purdue University, West Lafayette, IN, USA, in 2016.

He was awarded a Fulbright Scholarship for 2009–2011. He was a Supervisor of electrical maintenance with the Guangopolo Power Station, Guangopolo, Ecuador, from 2007 to 2009. He was also a Postdoctoral Research Assistant with Purdue University from 2016 to 2017. He is currently a Postdoctoral Researcher of power engineering with the National Renewable Energy Laboratory, Golden, CO, USA. His research interests include the intersection of renewable energy conversion, electrical power systems, systems control, and computational analysis of dynamical systems.

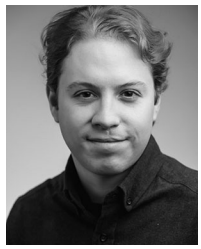

Brian B. Johnson (S'08–M'13) received the M.S. and Ph.D. degrees in electrical and computer engineering from the University of Illinois at Urbana–Champaign, Urbana, IL, USA, in 2010 and 2013, respectively. He is the Washington Research Foundation Innovation Assistant Professor with the Department of Electrical and Computer Engineering, University of Washington, Seattle, WA, USA. Prior to joining the University of Washington in 2018, he was an Engineer with the National Renewable Energy Laboratory, Golden, CO, USA. He was awarded a National Science Foundation Graduate Research Fellowship in 2010. His research interests are in renewable energy systems, power electronics, and control systems. He is an Associate Editor for the IEEE TRANSACTIONS ON ENERGY CONVERSION.